Soft Matter

PAPER

View Article Online
View Journal | View Issue

Check for updates

Cite this: *Soft Matter*, 2024, **20**, 6059

Elasto-inertial instabilities in the merging flow of viscoelastic fluids†

Mahmud Kamal Raihan,[a] Nayoung Kim,[a] Yongxin Song *[b] and Xiangchun Xuan *[a]

Received 17th June 2024,
Accepted 15th July 2024

DOI: 10.1039/d4sm00743c

rsc.li/soft-matter-journal

Many engineering and natural phenomena involve the merging of two fluid streams through a T-junction. Previous studies of such merging flows have been focused primarily upon Newtonian fluids. We observed in our recent experiment with five different polymer solutions a direct change from an undisturbed to either a steady vortical or unsteady three-dimensional flow at the T-junction with increasing inertia. The transition state(s) in between these two types of merging flow patterns is, however, yet to be known. We present here a systematic experimental study of the merging flow of polyethylene oxide (PEO) solutions with varying polymer concentrations and molecular weights. Two new paths of flow development are identified with the increase of Reynolds number: one is the transition in very weakly viscoelastic fluids first to steady vortical flow and then to a juxtaposition state with an unsteady elastic eddy zone in the middle and a steady inertial vortex on each side, and the other is the transition in weakly viscoelastic fluids first to a steady vortical and/or a juxtaposition state and then to a fully unsteady flow. Interestingly, the threshold Reynolds number for the onset of elastic instabilities in the merging flow is not a monotonic function of the elasticity number, but instead follows a power-law dependence on the polymer concentration relative to its overlap value. Such a dependence turns out qualitatively consistent with the prediction of the McKinley–Pakdel criterion.

1. Introduction

Viscoelastic polymer flows in microchannels are relevant in many fields such as oil recovery,[1,2] groundwater remediation,[3,4] blood characterization,[5] lab-on-a-chip applications,[6–10] *etc.* Numerous studies have been conducted in the past two decades to understand the elasto-inertial instabilities in these flows.[11–15] Many of them have been focused on flow fields with embedded re-entrant corners and/or stagnation points because they are profound at inducing elastic stresses and in turn instabilities.[16–33] A T-shaped junction is one such structure with a stagnation point pinned along the straight edge as well as two re-entrant corners on the bending edges. It has been frequently used for sample mixing[34,35] and sheath-focused particle/cell sorting,[36–39] where the incoming flows enter through the two side branches and merge in the main branch of a T-shaped microchannel (named as merging flow hereafter). The success of either of these microfluidic operations relies on a comprehensive understanding of the merging flow behavior at the T-junction. To date, however, most of the studies on this topic in the literature have been focused upon Newtonian fluids.[40–49] There are only a limited number of reports on how the fluid rheological properties may affect the merging flow of non-Newtonian fluids.

Perera and Walters[50] predicted a reduced pressure drop in the merging flow of an elastic fluid as compared to a Newtonian fluid. Nishimura *et al.*[51] observed secondary circulations in the merging flow of polyacrylamide (PAA) solution at the upstream sides of the re-entrant corners. Poole *et al.* predicted that fluid shear thinning either promotes or inhibits the bifurcation to asymmetric merging flow[52] while fluid elasticity draws flow instabilities at a lower Reynolds number than in a Newtonian fluid.[53] Soulages *et al.*[54] reported a direct transition of steady symmetric polyethylene oxide (PEO) flow to three-dimensional unsteady flow in a T-shaped microchannel at increasing Weissenberg number. Their observation agrees qualitatively with numerical simulation based on the simplified Phan–Thien–Tanner model. In a recent study our group investigated the effects of fluid rheological properties on the merging flow of five types of polymer solutions including polyvinylpyrrolidone (PVP), xanthan gum (XG), hyaluronic acid (HA), PEO and PAA.[55] We observed in these solutions a direct switch from an undisturbed flow to either a steady vortical or an unsteady three-dimensional flow near the stagnation point of the T-junction with the increase of Reynolds number, depending on the strength of fluid elasticity and/or shear thinning. The transition state in between these two types of merging flow patterns is, however, still unknown.

---

[a] Department of Mechanical Engineering, Clemson University, Clemson, SC 29634-0921, USA. E-mail: xcxuan@clemson.edu

[b] College of Marine Engineering, Dalian Maritime University, Dalian 116026, P. R. China. E-mail: yongxin@dlmu.edu.cn

† Electronic supplementary information (ESI) available. See DOI: https://doi.org/10.1039/d4sm00743c

This work is aimed to fill the knowledge gap through a systematic experimental study of the merging flow of viscoelastic PEO solutions through a planar T-shaped microchannel. By varying either the concentration or molecular weight of the polymer,[56,57] we can achieve a span of the fluid elasticity number over three orders of magnitude. We also vary the flow rate in each of the tested PEO solutions and achieve a span of both the Reynolds and Weissenberg numbers over two orders of magnitude. These wide ranges of parameters enable us to observe a full transition from the fluid inertia-induced vortical flow to the fluid elasticity-induced unsteady flow at the T-junction. We analyze the flow field images and compare the experimental data in dimensionless parameter spaces for a unified understanding.

2. Experiment

2.1. Materials

The T-shaped microchannel used in our recent study[55] was reused here providing the basis for a domain independent comparison of the results from the two projects. It was fabricated with polydimethylsiloxane (PDMS) using the standard soft lithography technique. The channel has an average depth of 50 μm with two 100 μm wide side branches of 8 mm long each and one 200 μm wide main branch of 10 mm long. We used neutrally charged and flexibly chained PEO (Sigma Aldrich) as our model polymer to prepare the viscoelastic solutions in deionized water (Thermo Fisher Scientific) for their well characterized properties in numerous previous works.[6–8,16,58,59] We chose 100 ppm PEO solution with 1 MDa molecular weight as the reference fluid. To investigate the polymer effect, we altered the concentration of PEO from 10 to 500 ppm or the average molecular weight of PEO from 0.3 to 8 MDa (nominal values as per the company). The PEO-free deionized water was also tested as a control experiment. The rheological properties of the prepared PEO solutions are summarized in Table 1. The overlap concentration, c^*, was obtained from the relationship,[60] $c^* = 1/[\eta]$, where $[\eta] = 0.072\ M_w^{0.65}$ is the intrinsic viscosity with M_w being the molecular weight of PEO polymer. All the PEO solutions have a small relative concentration, c/c^*, indicating to solutions being in their respective dilution regimes. Under this notion, their dynamic viscosities can be assumed to be shear independent and scale linearly with the relative polymer concentration,[60]

$$\eta = \eta_s(1 + c/c^*) \tag{1}$$

where η_s is the solvent (*i.e.*, water) viscosity. We note that eqn (1) predicts a viscosity value of $\eta = 2.17$ mPa s for 1000 ppm/2 MDa PEO solution ($c/c^* = 1.17$), nearly identical to our experimentally measured value,[24] which verifies the validity of using this equation. The relaxation times of the PEO solutions were each scaled *via* the Zimm theory,[60]

$$\lambda \propto [\eta]M_w(c/c^*)^{0.65} \propto c^{0.65}M_w^{2.0725} \tag{2}$$

and estimated from the experimentally measured $\lambda = 1.5$ ms for $c = 1000$ ppm and $M_w = 2$ MDa PEO solution in the literature.[58] This theory has been employed by several research groups[61–63] to estimate the relaxation time of PEO solutions, which exhibits a much stronger dependence on the PEO molecular weight (at an approximately second order) than the PEO concentration. We therefore see in Table 1 a nearly three orders of magnitude difference between the viscosities of 0.3 MDa and 8 MDa PEO solutions at 100 ppm because their molecular weights differ by almost 26 times.

Table 1 The rheological properties of the prepared PEO solutions

M_w (MDa)	c (ppm)	c^* (ppm)	$\frac{c}{c^*}$	η (mPa s)	λ (ms)	El
0.3	100	3820	0.0340	1.03	0.00658	0.00085
0.6	100	2440	0.0533	1.05	0.0277	0.0036
1	10	1750	0.00743	1.01	0.0179	0.0023
	30		0.0223	1.02	0.0365	0.0047
	50		0.0371	1.04	0.0509	0.0066
	100		0.0743	1.07	0.0798	0.011
	200		0.149	1.15	0.125	0.018
	300		0.223	1.22	0.163	0.025
	400		0.297	1.30	0.197	0.032
	500		0.371	1.37	0.227	0.039
2	100	1110	0.117	1.12	0.336	0.047
4	100	710	0.183	1.18	1.41	0.21
8	100	453	0.287	1.29	5.94	0.96

2.2. Methods

The flow pattern at the T-junction of the microchannel was visualized by seeding 1 μm diameter fluorescent polystyrene particles (Bangs Laboratories) at a concentration of 0.05% solid content into each of the prepared solutions. The particle suspension was driven through the microchannel from the two side branches by two identical syringe pumps (KD Scientific, Holliston, MA, USA) at equal flow rates. The streakline images of tracer particles were recorded using an inverted fluorescent microscope (Nikon Eclipse TE2000U) equipped with a CCD camera (Nikon DS-Qi1Mc) at a rate of 10–15 frames per second. The obtained images were processed using the Nikon imaging software (NIS-Elements AR 3.22). The effect of fluid inertia on the merging flow dynamics at the T-junction is characterized by the Reynolds number,

$$\mathrm{Re} = \frac{\rho V D_h}{\eta} = \frac{2\rho Q}{\eta(w+h)} \tag{3}$$

where ρ is the fluid density (assumed equal to that of water for all the solutions), $V = Q/wh$ is the average fluid velocity in the main branch of the channel with $D_h = 2wh/(w + h)$ being its hydraulic diameter, Q is the volumetric flow rate through the main branch, and w and h are the width and depth of the main branch, respectively. The effect of fluid elasticity is characterized by the Weissenberg number,

$$\mathrm{Wi} = \lambda\bar{\dot{\gamma}} = \frac{2\lambda Q}{w^2 h} \tag{4}$$

where $\bar{\dot{\gamma}} = 2V/w$ is the characteristic shear rate across the width of the main branch. The relative impact of the fluid elastic to inertial effect is measured by the elasticity number,

$$\mathrm{El} = \frac{\mathrm{Wi}}{\mathrm{Re}} = \frac{\lambda\eta(w+h)}{\rho w^2 h} \tag{5}$$

which is noteworthily independent of flow kinematics for constant viscosity fluids. The calculated values of El for our prepared PEO solutions, as presented in Table 1, are all less than unity but span over three orders of magnitude.

3. Results and discussion

3.1. Experimental images

3.1.1. Effect of polymer concentration. Fig. 1 shows the streakline images of tracer particles at the T-junction in the flow of PEO solutions with a range of concentrations from 10 to 500 ppm. The molecular weight of PEO polymer was kept at M_w = 1 MDa and the flow rate was varied from 1 to 120 mL h^{-1}. Similar to water (see the experimental images for the flow development in Section S-1 of the ESI†) in our recent study,[55] increasing the flow rate causes a transition from undisturbed to a state of symmetrically separated vortical zone in 10 ppm PEO solution. The vortex starting flow rate of 20 mL h^{-1} with Re = 44.2 can be marked as the onset of considerable inertial effect. The inertial vortices remain steady and symmetric, growing continually larger away from the spanwise center of the top-wall without any engulfment till the highest tested flow rate of 120 mL h^{-1} (Re = 265). To confirm the inertial flow characteristics in 10 ppm PEO solution, we conducted a three-dimensional simulation of water flow in COMSOL® under the experimental condition. The predicted streamlines in Fig. 1 (see the right half of the image for 60 mL h^{-1} in the top row) highlight the inertial vortices that visually match the streaklines of tracer particles (on the left half of the same image) in the flow of 10 ppm PEO solution. More details about our numerical model are presented in Section S-1 of the ESI.†

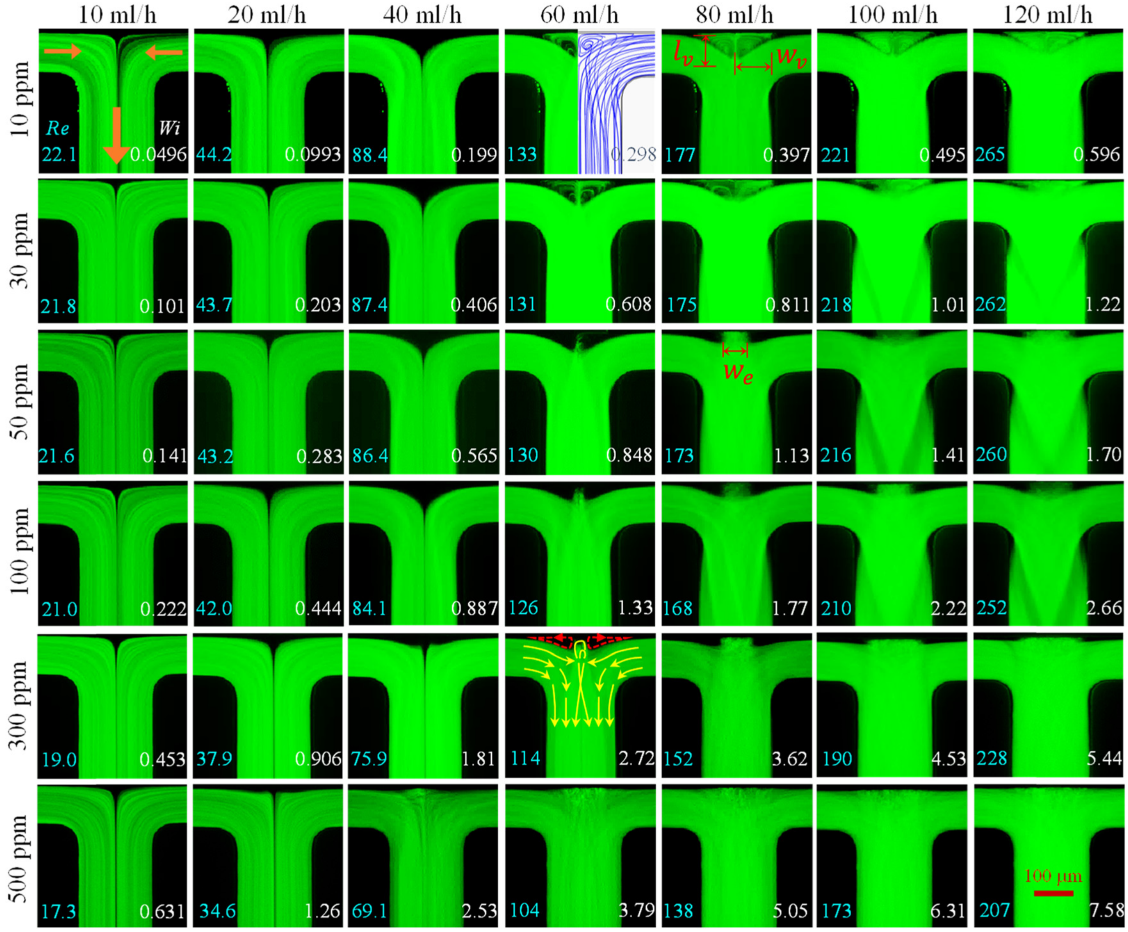

Fig. 1 Streakline images of tracer particles in the merging flow of PEO solutions with different concentrations (labeled to the left of images at each row) at various flow rates (labeled on top of the images at each column) through the T-junction of the microchannel. The corresponding Reynolds number and Weissenberg number are labeled on the left and right sides of the main branch on each image. The block arrows on the top-left image indicate the flow directions at the junction. The numerically predicted streamlines on the right half of the image in the top row (60 mL h^{-1} for 10 ppm PEO solution) illustrate the inertial vortices in the water flow. The labeled dimensions, l_v, w_v, and w_e on the images in the first and third rows indicate the measurement of the inertial vortex length, inertial vortex width, and elastic eddy zone width, respectively. The dashed- and solid-line arrows on the image in the second-to-the-bottom row highlight the steady inertial vortices and unsteady elastic eddy zone, respectively, in the juxtaposition state.

In 30 ppm PEO solution, however, increasing the flow rate to 90 mL h^{-1} (Re = 197 and Wi = 0.913) causes the streamlines near the cusp of inflow attachment to diverge unsteadily inwards the circulating zone. This deviation from the inertial feature signifies the impact of fluid elasticity because the free stagnant point at the cusp is the most promiscuous location for any elasticity induced breaking of stability to begin with.[11,12,15] Such an elasto-inertial instability occurs at 70 mL h^{-1} (Re = 151, data not shown in Fig. 1) in the more viscoelastic 50 ppm PEO solution, whereas the solutions with 100 ppm and above up to 300 ppm PEO encounter this state at even lower flow rates due to their increasingly stronger elasticity (see the increasing values of El in Table 1). The divergent streamlines in these PEO solutions become intense enough with the increasing flow rate to extend till the top wall, separating the contact between the inertial circulations. As a result, there exists a juxtaposition of an unsteady elastic eddy zone near the free stagnation point of the cusp and a steady inertial vortex on its each side in 50–300 ppm PEO solutions, which has not been reported in the literature on merging flows. Real-time videos of the streaklines of tracer particles in these solutions at the flow rate of 60 mL h^{-1} are available in the ESI.†

The elastic eddy zone becomes wider with the increasing inertia and gradually suppresses the inertial vortices on either side. A transition to (nearly) full suppression is observed in 300 ppm PEO solution at 120 mL h^{-1} (Re = 228), while 50–200 ppm PEO solutions all remain in the juxtaposition state till the highest tested flow rate. In contrast, 400 ppm and 500 ppm PEO solutions each show a transition from the undisturbed to juxtaposition state at 20 mL h^{-1} without going through the steady vortical flow and subsequently to a fully unsteady flow. The overlaying irregular streamlines at the T-junction only get accentuated without changing fundamentally in time fluctuations and spatial dimensions as the flow rate is increased. This unsteady regime at Re ≥ 34.6 signifies the combined effect of fluid elasticity and inertia. Such a phenomenon is different from the observation in 1000 ppm/2 MDa PEO solution (El = 0.37) in our recent study,[55] where the state of unsteady flow starts at a much smaller Re = 4.18, way before the fluid inertia plays a significant role. This variation

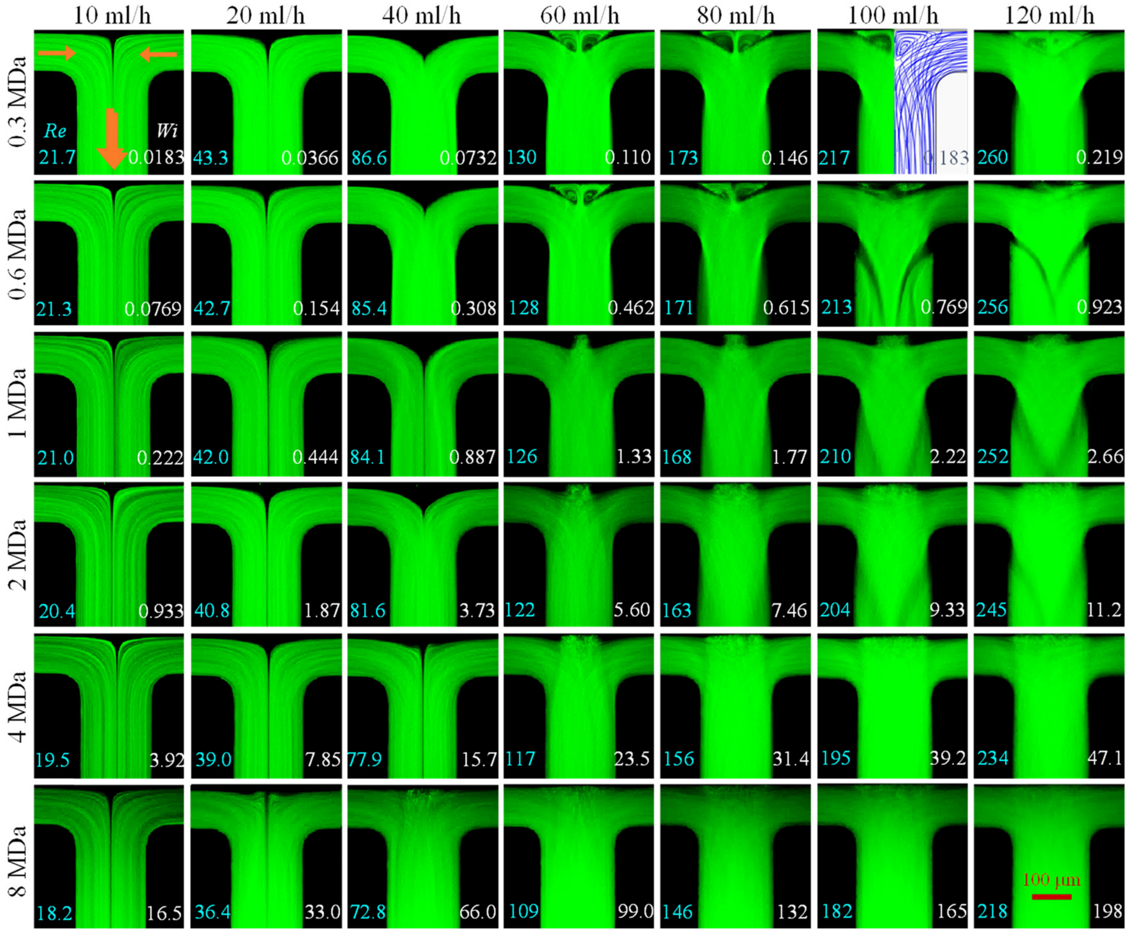

Fig. 2 Streakline images of tracer particles in the merging flow of 100 ppm PEO solutions with different molecular weights (labeled to the left of images at each row) at various flow rates (labeled on top of the images at each column) through the T-junction of the microchannel. The corresponding Reynolds number and Weissenberg number are labeled on the left and right sides of the main branch on each image. The block arrows on the top-left image indicate the flow directions at the junction. The numerically predicted streamlines on the right half of the image in the top row (100 mL h^{-1} for 0.3 MDa PEO solution) illustrate the inertial vortices in the water flow.

should be attributed to the much weaker elasticity of the fluids tested here (*e.g.*, El = 0.039 for the PEO solution with the highest concentration of 500 ppm).

3.1.2. Effect of polymer molecular weight. Fig. 2 shows the streakline images of tracer particles in the merging flow of 100 ppm PEO solutions with different M_w. The solution with the smallest M_w = 0.3 MDa shows a streamline development at the junction resembling that of 10 ppm/1 MDa PEO solution in Fig. 1. The flow also transitions from no disturbances to steady symmetric vortices at 20 mL h^{-1} with Re = 43.3, and the size of the latter steadily grows with the increasing inertia like. Such inertial flow characteristics in 0.3 MDa PEO solution are further confirmed by the similarity between the particle streaklines and the predicted streamlines in the flow of water at 100 mL h^{-1} in Fig. 2. Increasing M_w to 0.6 MDa causes little disparities from the flow events in the 0.3 MDa solution till 70 mL h^{-1} (Re = 149), at which the elasto-inertial instability is induced, akin to the case of 30 ppm/1 MDa PEO solution in Fig. 1. Further increasing M_w to 1 MDa leads to a flow pattern of transitioning first to steady symmetric circulations at around 20 mL h^{-1} and then to the juxtaposition state at 60 mL h^{-1} (Re = 126). In the 2 MDa and 4 MDa PEO solutions, the unsteady eddy zone in the latter state gets further enhanced at the same flow rate. It also grows faster in width along the top wall with increasing flow rates for higher M_w solutions, which transitions to the solely unsteady flow at 120 mL h^{-1} and 100 mL h^{-1} in the 2 MDa and 4 MDa PEO solutions, respectively. For the largest M_w case of 8 MDa, the merging flow transitions directly to the unsteady state at 20 mL h^{-1} (Re = 36.4) without an apparent juxtaposition state.

It is noted that the elasto-inertial instability in the 100 ppm/8 MDa PEO solution is again different from our recent observation in 1000 ppm/2 MDa solution, wherein, as noted earlier, the unsteady flow starts far before the fluid inertia takes effects.[55] As the PEO solution in our recent study actually has a smaller El = 0.37 than the 8 MDa solution (El = 0.96), we hypothesize that the polymer entanglement in terms of c/c^* (see Table 1) may play the primary role here and will discuss this aspect later in the paper. Another interesting phenomenon to note is that the juxtaposition and the subsequent unsteady states can be accessed by increasing either the flow rate (*i.e.*, fluid inertia in terms of Re as well as fluid elasticity in terms of Wi) or the polymer content including both concentration and M_w (*i.e.*, fluid elasticity in terms of El *via* the relaxation time). This phenomenon may be drawn upon the McKinley–Pakdel criterion,[64] which is expressed as,

$$M_{\text{crit}} = (\lambda V/\mathcal{R})_{\text{crit}} \tag{6}$$

where $\mathcal{R}$ is the curvature of a fluid path. Specifically, the M value can be incurred in the local flow region such that $M > M_{\text{crit}}$ by increasing either λ (through the increase of polymer concentration and/or molecular weight) or V (through the increase of flow rate) and hence imposing insufficient time for the relaxation and distribution of polymeric stresses on the path of traversal, invoking elastic instabilities. We will further discuss this aspect in the following sections through a quantitative analysis of all the experimental images and an integrated illustration in dimensionless parameter spaces.

3.2. Quantitative analyses

To quantify the effects of polymer concentration and M_w on the merging flow of PEO solutions, we measured from the images in Fig. 1 and 2 the length, l_v, and width, M_v, of the inertial vortices before the onset of juxtaposition state. Fig. 3(a) and (b) show the growth of the normalized (by the width of the main branch) vortex length, l_v/w, and vortex width, w_v/w, respectively, with respect to Re. Overall, a sigmoidal pattern, which has a slower growth in the low and high Re ends of the graph while a band of steeply increasing part in between, can be observed for both the length and width of inertial vortices. Moreover, the data points for each of these dimensions in every PEO solution illustrated in Fig. 3 collapse into the curve fitted for water. This phenomenon is consistent with that reported for the viscoelastic PVP (M_w = 0.36 MDa) and HA (M_w = 0.357 MDa) solutions in our recent study,[55] indicating the dominant role of fluid inertia

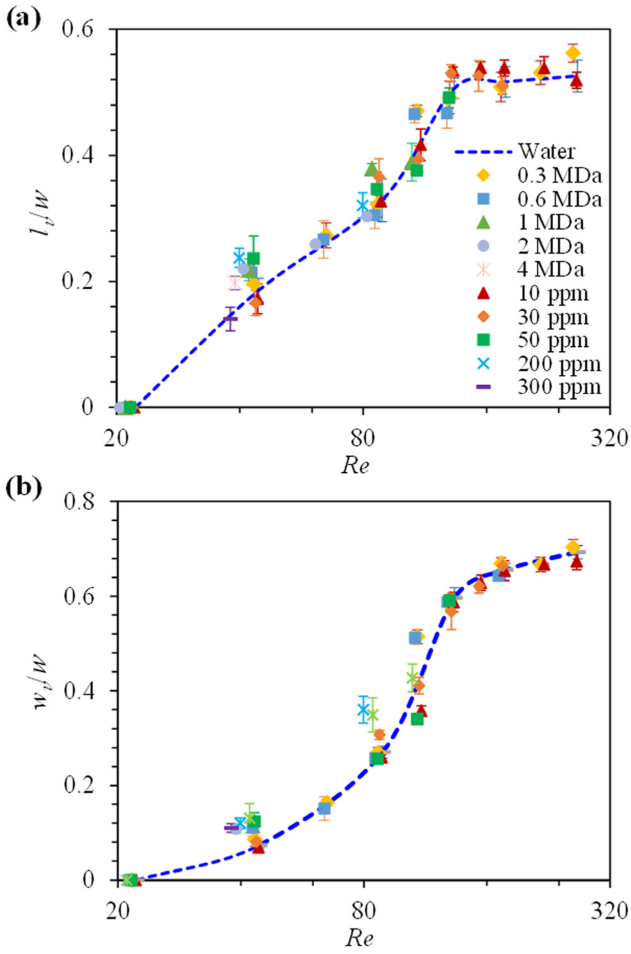

Fig. 3 Comparison of the inertial vortex development with Re before the onset of juxtaposition state in PEO solutions with varying polymer concentrations (for M_w = 1 MDa) or M_w (at 100 ppm): (a) normalized vortex length, l_v/w; (b) normalized vortex width, w_v/w. Error bars are included for all the data. The dashed lines connect the data points for water flow and are used here to guide the eyes only.

in the vortical flow over the fluid elasticity and shear-thinning effects. Note that Fig. 3 does not include the cases for 8 MDa or 400 and 500 ppm PEO solutions because of the absence of steady vortical flow therein.

We also measured from the images in Fig. 1 and 2 the width of the elastic eddy zone, w_e, in the juxtaposition state before the merging flow becomes fully unsteady. Fig. 4 shows the growth of the normalized (also by the width of the main branch) elastic eddy zone width, w_e/w, against Re in PEO solutions with varying concentrations or M_w. Overall, the curve for each case follows a roughly logarithmic dependence on Re. As the concentration or M_w is increased, the onset of the elastic eddy zone occurs earlier in Re because of the enhanced fluid elasticity effect in terms of the increasing value of El (see Table 1). The earliest onset takes place in 50 ppm/1 MDa solution (El = 0.0066) at Re = 130 whereas it is at Re = 97.4 in 100 ppm/4 MDa PEO solution (El = 0.21). The magnitude of w_e/w is also larger at any specific Re in higher El PEO solutions, further validating the elastic feature of the eddy zone in the juxtaposition state. Note that Fig. 4 does not include the cases for 0.3 and 0.6 MDa or 10 and 30 ppm PEO solutions, wherein the juxtaposition state does not appear.

3.3. Summary of flow regimes

Fig. 5 summarizes the flow regimes for our tested PEO solutions in the Re–Wl space, which is divided into four domains using three diagonal isolines at El ≈ 0.003, 0.03 and 0.3, respectively. The value of Wi = 0.01 is assigned to water at all flow rates for the sake of its inclusion to this plot. The vertical isoline at Re = 45 is also included on the plot to highlight the inertial domain, which was obtained from a three-dimensional simulation (COMSOL®) for the onset of inertial vortices in water flow and has been experimentally validated in our recent study.[55] In the negligibly elastic domain with El < 0.003, increasing the flow rate to around Re = 45 causes the flow at the T-junction to transition from a undisturbed state to inertial vortices in 100 ppm/0.3 MDa (El = 0.00085) and 10 ppm/1 MDa (El = 0.0023) PEO solutions despite the simultaneously increasing Wi. This phenomenon indicates that the fluid inertia effect dominates over the fluid elasticity effect in these two least viscoelastic PEO solutions. In the moderately elastic domain with El > 0.3 (including strongly elastic if El. > 1), increasing Re leads to a direct transition from undisturbed to fully unsteady flow in the mering flow of 100 ppm/8 MDa PEO solution. These two paths of merging flow development are consistent with the observations in our recent study.[55]

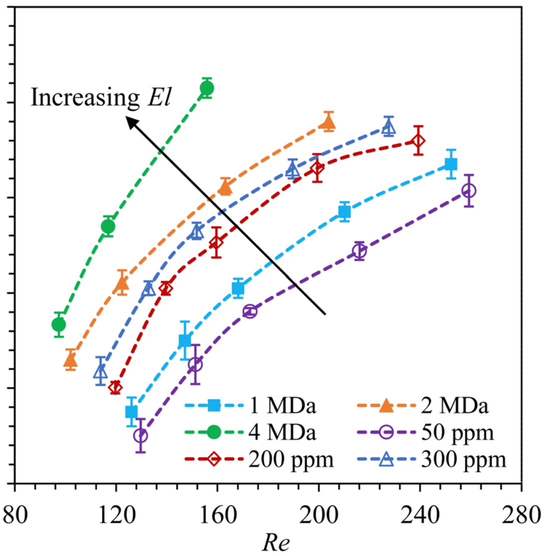

Fig. 4 Comparison of the normalized elastic eddy zone width, w_e/w, against Re in the juxtaposition state before the flow transitions to fully unsteady in PEO solutions with varying polymer concentrations (for M_w = 1 MDa) or M_w (at 100 ppm). The dashed lines are used here to guide the eyes only.

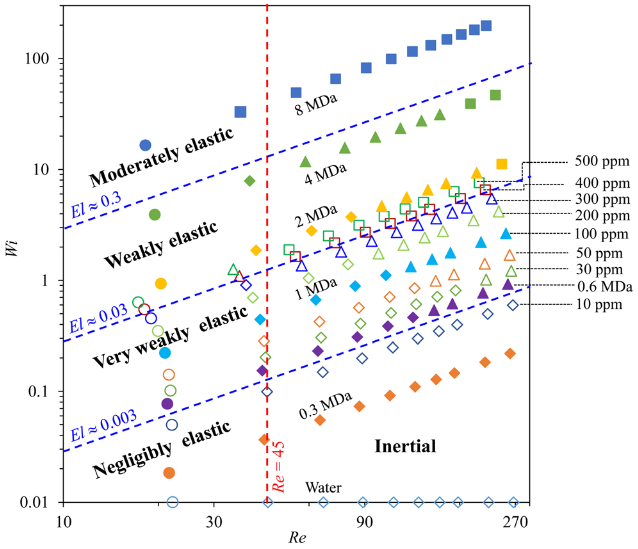

Fig. 5 Summary of the flow regimes observed in the merging flow of PEO solutions with varying polymer concentrations (for M_w = 1 MDa) or M_w (at 100 ppm) in the T-shaped microchannel: 'circles' for no flow disturbances, 'diamonds' for steady inertial vortices, 'triangles' for the juxtaposition of steady inertial vortices and unsteady elastic eddy zone, and 'rectangles' for unsteady flow. The diagonal dashed lines highlight the elasticity numbers and divide the whole space into four zones comprising the negligibly elastic (El < 0.003), very weakly elastic (0.003 ≤ El ≤ 0.03), weakly elastic (0.03 ≤ El ≤ 0.3), and moderately elastic (El > 0.3 including strongly elastic if El > 1) domains. The vertical dashed line highlights the Reynolds number, Re = 45, marking the start of the inertial domain wherein a steady vortical flow is induced at the T-junction in water.

In the very weakly elastic domain with 0.003 ≤ El ≤ 0.003, the merging flow of 30–300 ppm/1 MDa and 100 ppm/0.6 MDa PEO solutions transitions from undisturbed first to a steady vortical and then the juxtaposition state (which is unsteady due to the presence of elastic eddy zone) with the increase of Re. In the weakly elastic domain with 0.03 ≤ El ≤ 0.3, the merging flow transitions first to a juxtaposition state and then to a fully unsteady flow in 400 ppm (El = 0.032) and 500 ppm (El = 0.039)/1 MDa PEO solutions with the increase of Re. In the even more viscoelastic 100 ppm/2 MDa (El = 0.047) and 4 MDa (El = 0.21) PEO solutions, however, it transitions first to steady inertial vortices and subsequently to a juxtaposition state and then to a fully unsteady flow. This unexpected phenomenon in the

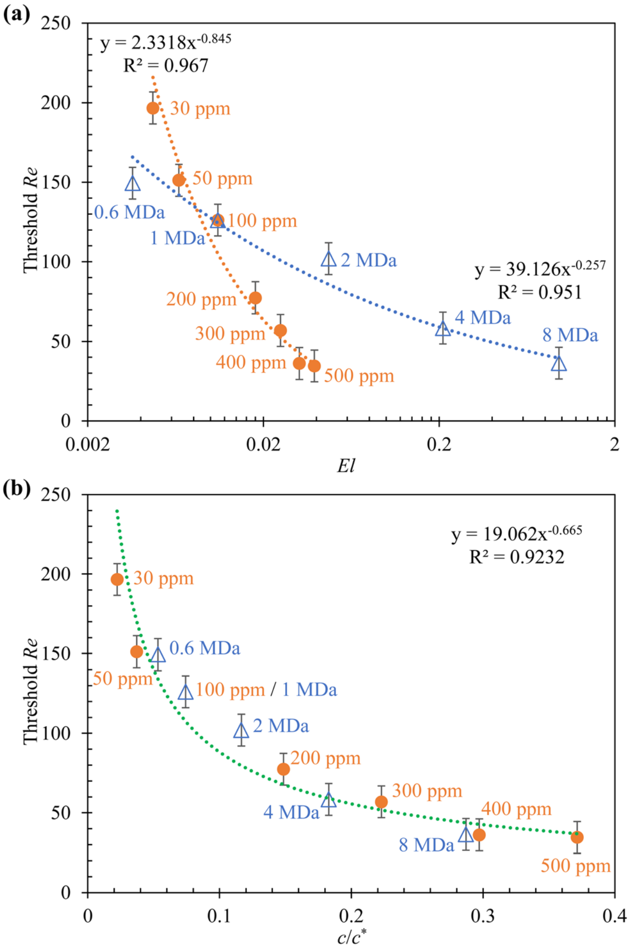

Fig. 6 Summary of the observed threshold Re for the onset of elastic instabilities in the merging flow of PEO solutions with varying polymer concentrations (for M_w = 1 MDa) or M_w (at 100 ppm) in terms of (a) El and (b) the relative polymer concentration, c/c^*. The dashed lines are each a power trendline fitted to the data points, for which the equation and R-squared value are displayed on the chart.

weakly elastic domain implies the role of another factor in the merging flow of viscoelastic fluids. None of the paths of flow development involving the juxtaposition state in the very weakly or weakly elastic domain has been reported in previous studies.

Referring to eqn (3) and (4), we can rewrite the McKinley–Pakdel criterion[64] in eqn (6) as,

$$M_{\mathrm{crit}} = \left(\frac{\rho V D_{\mathrm{h}}}{\eta}\frac{\lambda\eta}{\rho D_{\mathrm{h}}\mathcal{R}}\right)_{\mathrm{crit}} = \left(\mathrm{ReEl}\frac{w}{2\mathcal{R}}\right)_{\mathrm{crit}} \tag{7}$$

This form of M_{crit} indicates an inverse relationship between the threshold Re for the onset of elastic instabilities (in the form of either diverging streamlines for 30 ppm/1 MDa and 100 ppm/0.6 MDa, juxtaposition state for 50–500 ppm/1 MDa and 100 ppm/1–4 MDa, or fully unsteady flow for 100 ppm/8 MDa) and the value of El. Fig. 6(a) shows the experimentally observed threshold Re against El in the PEO solutions with varying polymer concentrations and molecular weights, respectively. The data points for each parametric case can be best fitted to a power trendline, whose index (see the equations displayed on the chart), however, deviates from the prediction of eqn (7). The inclusion of the contribution of solvent viscosity into M_{crit}, which, as suggested by McKinley *et al.*[65] because of its stabilizing effect on the onset of purely elastic instabilities, does not seem to improve the agreement in either case (see Fig. S-3 and the additional analysis in terms of Wi in Section S-2 of the ESI†). The experimentally observed values of threshold Re in all the PEO solutions under test are replotted in Fig. 6(b) as a function of the relative polymer concentration, c/c^* (see Table 1). A power-law dependence with an index of −0.665 (see the equation displayed on the chart) is obtained, which appears to closely match the dependence of the fluid relaxation time, λ, on c/c^* in eqn (2). This correlation turns out qualitatively consistent with the McKinley–Pakdel criterion[64] in the following scaling form *via* the use of eqn (2) and (3) in eqn (6),

$$M_{\mathrm{crit}} \propto (c/c^*)^{0.65}\mathrm{Re} \tag{8}$$

It also points to the significance of polymer entanglement in the merging flow of viscoelastic fluids, which may share a similar origin to the recent observations of c/c^* dependent electro-elastic migration of particles in PEO solutions.[66,67]

We also note that the iso-El line in Fig. 5 for the negligibly elastic domain is two orders of magnitude smaller than the value, El ≈ 0.3, identified between the steady vortical flow in PVP (10 000 ppm/0.36 MDa, El = 0.16) & HA (1000 ppm/0.357 MDa, El = 0.010) solutions and the unsteady flow in PEO (1000 ppm/2 MDa, El = 0.37) & PAA (200 ppm/18 MDa, El = 27) solutions in our recent study.[55] Such a large discrepancy perhaps indicates a more important role of polymer M_w than concentration in the merging flow of viscoelastic fluids, which seems consistent with the fluid relaxation time in the Zimm theory given by eqn (2). This hypothesis may also be used to explain why even the negligibly elastic XG solution (2000 ppm/2 MDa) can undergo the unsteady flow[55] because of its large polymer M_w. In addition, we note that the observed threshold Re = 4.18 for the onset of elastic instabilities in 1000 ppm/2 MDa PEO solution (c/c^* = 1.17) in our recent study[55] is much smaller than the lowest value of Re = 34.6 for 500 ppm/1 MDa PEO solution (c/c^* = 0.371, see Table 1) in this work. This comparison turns out to be consistent with the fitted trendline in Fig. 6(b).

4. Conclusions

We have experimentally studied the elasto-inertial instabilities in the merging flow of PEO solutions with varying polymer concentrations and molecular weights over a wide range of flow rates. The observed flow regimes in each of these solutions are summarized in the dimensionless Re-Wi space that can be divided into four domains based on the value of El. Specifically, the merging flow transitions from the undisturbed directly to steady vortical and unsteady overlaying states in the negligibly elastic (El < 0.003) and moderately elastic (El > 0.3 including strongly elastic if $\mathrm{El} > 1$) domains, respectively, qualitatively consistent with those reported in our recent study.[55] Two new paths of merging flow development are identified in the very weakly elastic ($0.003 \le \mathrm{El} \le 0.03$) and weakly elastic ($0.03 \le \mathrm{El} \le 0.3$) domains, where the former transitions first to a steady vortical and then to a juxtaposition state while the latter transitions first to a steady vortical and/or a juxtaposition state and then to a fully unsteady flow. We find that the development of inertial vortex size with Re before the juxtaposition state occurs in all the tested PEO solutions, if applicable, collapses into the curve for water. The width of the elastic eddy zone before the merging flow transitions to fully unsteady increases in higher-El PEO solutions for the same Re. However, the threshold Re for the onset of elastic instabilities is not a monotonic function of El, but instead follows a power-law dependence on the relative polymer concentration, c/c^*, qualitatively consistent with the McKinley–Pakdel criterion.[64] Our experimental results in this work advance the understanding of merging flow instabilities due to fluid elasticity. They are expected to enrich the database for the validation and calibration of numerical models for non-Newtonian fluid flows.[68]

Author contributions

M. K. R. and N. K. performed the experiment; M. K. R. conducted the analysis of experimental data; Y. S. and X. X. designed and supervised the project; M. K. R. wrote the manuscript; X. X. edited the manuscript; all authors commented on the manuscript.

Data availability

The data supporting this article have been included as part of the ESI.†

Conflicts of interest

None.

Acknowledgements

This work was supported in part by Clemson University through the Creative Inquiry and Departmental Honors Programs (X. X.), and University 111 Project of China under grant number B08046 (Y. S.).

References

1 A. Mohsenatabar Firozjaii and H. R. Saghafi, *Petroleum*, 2020, **6**, 115–122.
2 R. Farajzadeh, S. Kahrobaei, A. A. Eftekhari, R. A. Mjeni, D. Boersma and J. Bruining, *Sci. Rep.*, 2021, **11**, 829.
3 R. Mosler and T. A. Hatton, *Curr. Opin. Colloid Interface Sci.*, 1996, **1**, 540–547.
4 A. C. Barbati, J. Desroches, A. Robisson and G. H. McKinley, *Annu. Rev. Chem. Biomol. Eng.*, 2016, **7**, 415–453.
5 S. A. Wajihah and D. S. Sankar, *Arch. Appl. Mech.*, 2023, **93**, 1771–1796.
6 X. Lu, C. Liu, G. Hu and X. Xuan, *J. Colloid Interfaces Sci.*, 2017, **500**, 182–201.
7 D. Yuan, Q. Zhao, S. Yan, S. Tang, G. Alici, J. Zhang and W. Li, *Lab Chip*, 2018, **18**, 551–567.
8 J. Zhou and I. Papautsky, *Microsys. Nanoeng.*, 2020, **6**, 113.
9 Y. Song, D. Li and X. Xuan, *Electrophoresis*, 2023, **44**, 910–937.
10 F. Shen, J. Gao, J. Zhang, M. Ai, H. Gao and Z. Liu, *Biomicrofluid*, 2024, **18**, 021504.
11 M. A. Alves and R. J. Poole, *J. Non-Newtonian Fluid Mech.*, 2007, **144**, 140–148.
12 F. J. Galindo-Rosales, L. Campo-Deaño, P. C. Sousa, V. M. Ribeiro, M. S. N. Oliveira, M. A. Alves and F. T. Pinho, *Exp. Therm. Fluid Sci.*, 2014, **59**, 128–139.
13 A. Anbari, H. T. Chien, S. S. Datta, W. Deng, D. A. Weitz and J. Fan, *Small*, 2018, **14**, 1703575.
14 C. A. Browne, A. Shih and S. S. Datta, *Small*, 2020, **16**, 1903944.
15 S. S. Datta, A. M. Ardekani, P. E. Arratia, A. N. Beris, I. Bischofberger, G. H. McKinley, J. G. Eggers, J. E. López-Aguilar, S. M. Fielding, A. Frishman, M. D. Graham, J. S. Guasto, S. J. Haward, A. Q. Shen, S. Hormozi, A. Morozov, R. J. Poole, V. Shankar, E. S. G. Shaqfeh, H. Stark, V. Steinberg, G. Subramanian and H. A. Stone, *Phys. Rev. Fluids*, 2022, **7**, 080701.
16 L. E. Rodd, J. J. Cooper-White, D. V. Boger and G. H. McKinley, *J. Non-Newtonian Fluid Mech.*, 2007, **143**, 170–191.
17 L. Campo-Deañoa, F. J. Galindo-Rosales, F. T. Pinho, M. A. Alves and M. S. N. Oliveira, *J. Non-Newtonian Fluid Mech.*, 2011, **166**, 1286–1296.
18 A. Lanzaro, Z. Li and X. F. Yuan, *Microfluid. Nanofluid.*, 2015, **18**, 819–828.
19 S. J. Haward, J. Page, T. A. Zaki and A. Q. Shen, *Phys. Fluids*, 2018, **30**, 113101.
20 R. M. Matos, M. A. Alves and F. T. Pinho, *Exp. Fluids*, 2019, **60**, 145.
21 K. Zografos, W. Hartt, M. Hamersky, M. S. N. Oliveira, M. A. Alves and R. J. Poole, *J. Non-Newtonian Fluid Mech.*, 2020, **278**, 104222.
22 C. A. Browne, A. Shih and S. S. Datta, *J. Fluid Mech.*, 2020, **890**, A2.
23 M. Kumar, S. Aramideh, C. A. Browne, S. S. Datta and A. M. Ardekani, *Phys. Rev. Fluids*, 2021, **6**, 033304.
24 M. K. Raihan, S. Wu, Y. Song and X. Xuan, *Soft Matter*, 2021, **17**, 9198–9209.
25 C.-D. Xue, Z.-Y. Zheng, G.-S. Zhang, D.-W. Zhao and K.-R. Qin, *Soft Matter*, 2022, **18**, 3867–3877.
26 C. C. Hopkins, S. J. Haward and A. Q. Shen, *Soft Matter*, 2022, **18**, 4868–4880.
27 M. K. Raihan, S. Wu, H. Dort, M. Baghdady, Y. Song and X. Xuan, *Soft Matter*, 2022, **18**, 7427–7440.

28 C. C. Hopkins, A. Q. Shen and S. J. Haward, *Soft Matter*, 2022, **18**, 8856–8866.
29 F. Khalkhal and S. Muller, *Phys. Rev. Fluids*, 2022, **7**, 023303.
30 M. Kumar, D. M. Walkama, A. M. Ardekani and J. S. Guasto, *Soft Matter*, 2023, **19**, 6761–6770.
31 D. W. Carlson, A. Q. Shen and S. J. Haward, *J. Non-Newtonian Fluid Mech.*, 2024, **323**, 105169.
32 A. Yokokoji, S. Varchanis, A. Q. Shen and S. J. Haward, *Soft Matter*, 2024, **20**, 152–166.
33 X. Y. Xu, Z. Y. Zheng, K. Tian, D. Wang, K. R. Qin and C. D. Xue, *Phys. Fluids*, 2024, **36**, 042001.
34 C.-Y. Lee, W.-T. Wang, C.-C. Liu and L.-M. Fu, *Chem. Eng. J.*, 2016, **288**, 146–160.
35 S. M. Saravanakumar and P.-V. Cicek, *Micromachines*, 2023, **14**, 1827.
36 X. Lu and X. Xuan, *Anal. Chem.*, 2015, **87**, 11523–11530.
37 K. Kang, S. S. Lee, K. Hyun, S. J. Lee and J. M. Kim, *Nat. Commun.*, 2013, **4**, 2567.
38 D. Yuan, S. H. Tan, R. Sluyter, Q. Zhao, S. Yan, N. T. Nguyen, J. Guo, J. Zhang and W. Li, *Anal. Chem.*, 2017, **89**, 9574–9582.
39 S. Yan, Y. Liu, N.-T. Nguyen and J. Zhang, *Anal. Chem.*, 2024, **96**, 3925–3932.
40 M. Engler, N. Kockmann, T. Kiefer and P. Woias, *Chem. Eng. J.*, 2004, **101**, 315–322.
41 M. Hoffmann, M. Schlüter and N. Räbiger, *Chem. Eng. Sci.*, 2006, **61**, 2968–2976.
42 A. Soleymani, H. Yousefi and I. Turunen, *Chem. Eng. Sci.*, 2008, **63**, 5291–5297.
43 S. K. Reddy Cherlo and S. Pushpavanam, *Chem. Eng. Sci.*, 2010, **65**, 6486–6490.
44 A. Fani, S. Camarri and M. V. Salvetti, *Phys. Fluids*, 2013, **25**, 064102.
45 A. Fani, S. Camarri and M. V. Salvetti, *Phys. Fluids*, 2014, **26**, 074101.
46 T. Andreussi, C. Galletti, R. Mauri, S. Camarri and M. V. Salvetti, *Comput. Chem. Eng.*, 2015, **76**, 150–159.
47 A. Mariotti, C. Galletti, R. Mauri, M. V. Salvetti and E. Brunazzi, *Chem. Eng. J.*, 2018, **341**, 414–431.
48 V. S. T. Madana and B. A. Ali, *Phys. Fluids*, 2020, **32**, 07200.
49 S. Camarri, A. Mariotti, C. Galletti, E. Brunazzi, R. Mauri and M. V. Salvetti, *Ind. Eng. Chem. Res.*, 2020, **59**, 3669–3686.
50 M. G. N. Perera and K. Walters, *J. Non-Newtonian Fluid Mech.*, 1977, **2**, 49–81.
51 T. Nishimura, K. Nakamura and A. Horikawa, *J. Text. Mach. Soc. Jpn.*, 1985, **31**, 1–6, DOI: **10.4188/jte1955.31.1**.
52 R. J. Poole, M. Alfateh and A. P. Gauntlett, *Chem. Eng. Sci.*, 2013, **104**, 839–848.
53 R. J. Poole, S. J. Haward and M. A. Alves, *Procedia Eng.*, 2014, **79**, 28–34.
54 J. Soulages, M. S. N. Oliveira, P. C. Sousa, M. A. Alves and G. H. McKinley, *J. Non-Newtonian Fluid Mech.*, 2009, **163**, 9–24.
55 L. Song, M. K. Raihan, L. Yu, S. Wu, N. Kim, S. Till, Y. Song and X. Xuan, *Soft Matter*, 2023, **19**, 3207–3214.
56 M. K. Raihan, M. Baghdady, H. Dort, J. Bentor and X. Xuan, *Anal. Chem.*, 2023, **95**, 16013–16020.
57 J. Bentor and X. Xuan, *Anal. Chem.*, 2024, **96**, 3186–3191.
58 L. E. Rodd, T. P. Scott, D. V. Boger, J. J. Cooper-White and G. H. McKinley, *J. Non-Newtonian Fluid Mech.*, 2005, **129**, 1–22.
59 S. Wu, M. K. Raihan, L. Song, X. Shao, J. B. Bostwick, L. Yu, X. Pan and X. Xuan, *J. Non-Newtonian Fluid Mech.*, 2021, **290**, 104508.
60 V. Tirtaatmadja, H. G. McKinley and J. J. Cooper-White, *Phys. Fluids*, 2006, **18**, 043101.
61 F. Tian, L. Cai, J. Chang, S. Li, C. Liu, T. Li and J. Sun, *Lab Chip*, 2018, **18**, 3436–3445.
62 Y. Zhou, Z. Ma and Y. Ai, *Lab Chip*, 2020, **20**, 568–581.
63 P. Liu, H. Liu, D. Yuan, D. Jang, S. Yan and M. Li, *Anal. Chem.*, 2021, **93**, 1586–1595.
64 P. Pakdel and G. H. McKinley, *Phys. Rev. Lett.*, 1996, **77**, 2459–2462.
65 G. H. McKinley, P. Pakdel and A. Oztekin, *J. Non-Newtonian Fluid Mech.*, 1996, **67**, 19–47.
66 M. Serhatlioglu, Z. Isiksacan, M. Ozkan, D. Tuncel and C. Elbuken, *Anal. Chem.*, 2020, **92**, 6932–6940.
67 D. Li and X. Xuan, *Phys. Fluids*, 2023, **35**, 092013.
68 M. A. Alves, P. J. Oliveira and F. T. Pinho, *Annu. Rev. Fluid Mech.*, 2021, **53**, 509–541.